Biochemistry and Biophysics Reports 38 (2024) 101712

Contents lists available at ScienceDirect

Biochemistry and Biophysics Reports

journal homepage: www.elsevier.com/locate/bbrep

Micro-second time-resolved X-ray single-molecule internal motions of SARS-CoV-2 spike variants

Daisuke Sasaki [a,b], Tatsuya Arai [a,b], Yue Yang [a,b], Masahiro Kuramochi [c], Wakako Furuyama [d], Asuka Nanbo [d], Hiroshi Sekiguchi [e], Nobuhiro Morone [f], Kazuhiro Mio [b], Yuji C. Sasaki [a,b,e,*]

[a] Graduate School of Frontier Sciences, The University of Tokyo, 5-1-5 Kashiwanoha, Kashiwa, Chiba, 277-8561, Japan
[b] AIST-UTokyo Advanced Operando-Measurement Technology Open Innovation Laboratory (OPERANDO-OIL), National Institute of Advanced Industrial Science and Technology (AIST), Kashiwa, Chiba, 277-0882, Japan
[c] Graduate School of Science and Engineering, Ibaraki University, 4-12-1 Naka-narusawa, Hitachi, Ibaraki, 316-8511, Japan
[d] National Research Center for the Control and Prevention of Infectious Diseases, Nagasaki University, 1-12-4 Sakamoto, Nagasaki, Nagasaki, 852-8523, Japan
[e] Center for Synchrotron Radiation Research, Japan Synchrotron Radiation Research Institute, 1-1-1 Kouto, Sayo, Hyogo, 679-5198, Japan
[f] MRC Toxicology Unit, University of Cambridge, Gleeson Building, Tennis Court Road, Cambridge, CB2 1QR, UK

ARTICLE INFO

Keywords:
Diffracted X-ray tracking
SARS-CoV-2 spike protein
Single-molecule internal dynamics
Micro-second time-resolved measurement

ABSTRACT

Single-molecule intramolecular dynamics were successfully measured for three variants of SARS-CoV-2 spike protein, alpha: B.1.1.7, delta: B.1.617, and omicron: B.1.1.529, with a time resolution of 100 μs using X-rays. The results were then compared with respect to the magnitude and directions of motions for the three variants. The largest 3-D intramolecular movement was observed for the omicron variant irrespective of ACE2 receptor binding. A more detailed analysis of the intramolecular motions revealed that the distribution state of intramolecular motion for the three variants was completely different with and without ACE2 receptor binding. The molecular dynamics for the trimeric spike protein of the omicron variant increased when ACE2 binding occurred. At that time, the diffusion constant increased from 71.0 [mrad^2/ms] to 91.1 [mrad^2/ms].

1. Introduction

In late 2019, severe acute respiratory syndrome coronavirus 2 (SARS-CoV-2), which is an enveloped virus with spike proteins on the viral surface, emerged in Wuhan, China, and lead to the worldwide COVID-19 pandemic [1]. SARS-CoV-2 has developed various variants [2–4], and despite the development of vaccines, the infection is still spreading as of 2023. The SARS-CoV-2 spike protein binds with ACE2 before viral entry into cells [5,6], similar to the SARS-CoV spike protein [7]. The structures of the spike variants has been reported, as well as the binding of ACE2 to the receptor binding domain (RBD) from SARS-CoV-2 [8–11]. In addition, the spike protein, which contains three flexible hinges, moves frequently over a wide range [12]. The binding mode of its central molecule, the spike protein molecule, to the ACE2 receptor and its binding stability have attracted much attention. By measuring the intramolecular motions of these molecules, it is possible to consider information such as the binding modes. Several single-molecule measurement methods are available to measure the intramolecular motion of proteins immobilized on a substrate, such as single-molecule fluorescence resonance energy transfer (sm-FRET) [13,14], atomic force microscopy (AFM) [15–17], classical molecular dynamics (MD) simulation [18,19] and Density Functional Tight Binding (DFTB) [20,21].

Classical MD simulations enable calculations for large-scale systems, but DFTB offers advantages in terms of accuracy and computational cost. The sm-FRET timescale and the AFM timescale range from milliseconds to seconds. Among these measurements, performing single-molecule measurements using X-rays is the most accurate and fastest method for measuring the internal motion of molecules. The results represent real-time measurements that are closest to the timescale of MD simulations and DFTB, ranging from picoseconds to microseconds. This method, called Diffracted X-ray Tracking (DXT) [22–27], has been used to detect the intramolecular motion of many membrane proteins [25,26]. In particular, DXT can determine the directionality of rotational motion and measure the angle of change in 10–100 μs per frame.

* Corresponding author. Department of Advanced Materials Science, Graduate School of Frontier Sciences, The University of Tokyo, 7H8 #609 Kiban Bldg., 5-1-5 Kashiwanoha, Kashiwa, Chiba, 277-8561, Japan.
E-mail address: ycsasaki@edu.k.u-tokyo.ac.jp (Y.C. Sasaki).

https://doi.org/10.1016/j.bbrep.2024.101712
Received 23 October 2023; Received in revised form 9 April 2024; Accepted 13 April 2024
Available online 29 April 2024

2. Results & discussion

In this study, we performed 100 μs time-resolved DXT measurements of three SARS-CoV-2 spike variants for two different molecular arrangements, as shown in Fig. 1A The first molecular arrangement consisted of a His-tagged SARS-CoV-2 spike trimer immobilized on a polyimide substrate via Co^{2+}, and gold nanocrystals attached to the cysteine of the immobilized spike protein [28]. The next molecular arrangement was obtained by first immobilizing the SARS-CoV-2 spike trimer on a polyimide substrate and then allowing it to react with angiotensin converting enzyme 2 (ACE2). Since ACE2 has an Fc-tag at its C-terminus, it was labelled with protein A/G-coated gold nanocrystals; ACE2 binds to the receptor binding domain (RBD) of the spike protein.

Diffracted X-ray Tracking (DXT) is an X-ray-based single-molecule technique, as shown in Fig. 1B (PDB ID Spike Protein: 7CWL [29], ACE2: 7l7f [30], Fc-tag: 6g1e [31]). Other molecular arrangements are not suitable for measuring the internal motion of spike proteins. The details of the internal dynamics are not measured well enough for the arrangement of cysteines in the spike protein bound to a substrate (Fig. S1) because the gold nanocrystals and the interaction site are too far apart. In another arrangement, ACE2 is immobilized on a substrate and interacts with spike protein-labelled gold nanocrystals via a His-tag (Fig. S2). In this case, although the internal dynamics of the decomposition process of the virus are measured, the results are not suitable for this research because the purpose of this research is to measure the internal motion of the spike protein during the process of infection. An arrangement of gold nanocrystal-binding spike proteins interacting with ACE2 (Fig. S3A) is suitable for measuring the difference in dynamics before and after ACE2 binding. However, due to this arrangement, the binding efficiency of gold nanocrystals to the spike protein is lower than in the arrangement of gold nanocrystals attached to ACE2 via the Fc-tag (Fig. S3B). Therefore, because the arrangement in Fig. S3B enabled us to measure the internal dynamics of cell invasion, the experiments were performed with this arrangement. In the experiment, the side view of spike proteins binding to ACE2 with gold nanocrystals to be measured is shown in Fig. 1C. The spike proteins can move around the immobilized point on the substrate in the aqueous solution. The internal dynamics of individual adsorbed protein molecules on the substrate can be indirectly measured through the trajectory of Laue diffraction spots from gold nanocrystals with a diameter of 60–80 nm bound to the adsorbed protein molecule. In the arrangement without ACE2, gold nanocrystals bind to cysteine residues that do not participate in disulfide bonds [32]. On the other hand, in the arrangement with ACE2, the RBD of the spike protein interacts with gold nanoparticles attached to ACE2 (Fig. S4). The diffraction spots were observed with incident X-rays in the energy range of 14.0–16.5 keV, with measurements taken in 500 frames at a frame rate of 100 μs. The trajectories in two directions, tilting (θ) and twisting (χ), were analyse [25,26]. Dynamics of biomolecular structures span various timescales, ranging from femtoseconds to seconds, encompassing processes from fast to slow dynamics [33,34]. In this study, we successfully measured the molecular dynamics of domains containing the RBD of the spike protein, as well as the interaction dynamics between the RBD and the ACE2 binding domain, with a time resolution of 100 μs.

Fig. 1D shows examples for the experiments tracking the motion of a time-resolved Laue diffraction spot resolved in the following directions: tilt (θ) and twist (χ). The trajectory of the green spot shows a large displacement in the θ direction and a slight shift in the χ direction. The internal dynamics of the protein molecule labelled with the gold nanocrystal, corresponding to the green spot, roughly move more in the tilting direction than in the twist direction. Strictly speaking, real space and reciprocal lattice space are also different spaces when considering the motion width. However, when the motion width is very narrow, as for DXT data, this interpretation is intuitive and easy to understand. On the other hand, the trajectory of the purple spot is an example of greater movement in the χ direction than in the θ direction. Finally, the trajectory of the blue spot moves at approximately the same rate in the χ and θ directions and to the same extent in the tilting and twisting

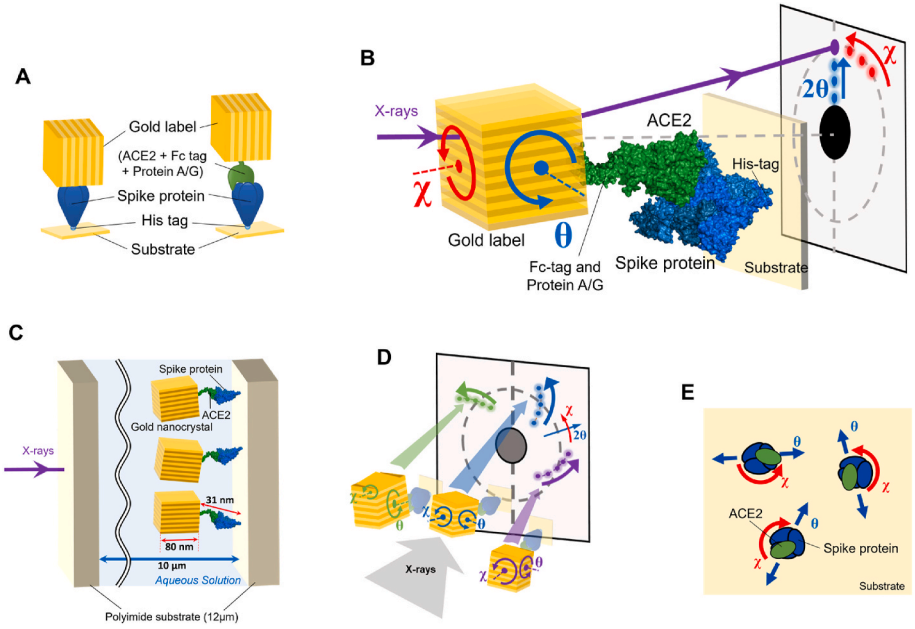

Fig. 1. DXT measurement models of SARS-CoV-2 spike protein trimer bound to ACE2. **A:** Schematic view of a His-tagged SARS-CoV-2 spike trimer stabilized on a polyimide substrate via a cobaltous cation and a gold nanocrystal attached to the top of the trimer (left) and ACE2 attached to a gold nanocrystal via Fc-tag binding to spike RBD (right). **B:** Schematic view of DXT measurement of spike trimer (blue) bound to ACE2 (green) attached to a gold nanocrystal. The tilting (θ) and twisting (χ) directions observed by DXT. **C:** Schematic cross section of the samples immobilized on a polyimide substrate and labelled with gold nanocrystals. **D:** Schematic view of diffraction spot trajectories in time-resolved observations. The green diffraction spots move in the tilting (θ) direction with a tendency towards the twisting (χ) direction. The purple spots move in the twisting (χ) direction with a tendency towards the tilting (θ) direction. The blue spots move equally in tilting (θ) and twisting (χ) directions. **E:** Schematic view of the top view of the SARS-CoV-2 spike trimer with ACE2. (For interpretation of the references to colour in this figure legend, the reader is referred to the Web version of this article.)

motions.

Fig. 1E shows a schematic top view of the SARS-CoV-2 spike trimer bound to ACE2 immobilized on a polyimide substrate. Since all His-tagged sites of the SARS-CoV-2 spike trimer are adsorbed on the substrate side, it is possible to distinguish twisting into positive and negative directions. However, since the molecules are randomly adsorbed in two dimensions, the tilting direction (θ direction) cannot be discussed in terms of positive or negative directionality, only absolute momentum. This feature of the DXT results for these angles (χ and θ) is very important; thus, it is specified in Fig. 1E.

Fig. 2A shows an actual stacking image of diffraction spots obtained from DXT measurements. We established a blue θ-axis extending outward from the center of the diffraction ring and a red χ-axis aligned with the rotation along the diffraction ring. The plane spacing of the Au (111) plane with a value of 2.35 Å appears in the inner region, while the Au (200) plane with a plane spacing of 2.04 Å is also observed outward. It is possible to continuously capture and track these diffraction spots throughout the acquisition, when the spots move in the 2θ direction, because of the X-rays with energy widths ranging from 14.0 to 16.5 keV. We illustrated an example of diffraction spot tracking in Fig. 2B. The diffraction spot located at the center of the image at $\Delta t = 0.0$ ms moves at intervals of $\Delta t = 0.5$ ms and eventually shifts to the upper right corner of the image at $\Delta t = 2.0$ ms. The image, obtained by accumulating frames from $\Delta t = 0.0$–2.0 ms, is shown in the rightmost panel. We calculate the angular displacement in two directions, namely, the 2θ and χ directions, in response to the movement of this spot. Fig. 2C shows the angular displacements in the θ and χ directions for each diffraction spot and plotted them in a three-dimensional representation for the frames where the spots were observed. We also presented an image where the angular displacements in the two directions are stacked over frames between 250 and 270, with the "frame number" axis. The left 3d plot of Fig. 2C represents the plotted angular displacements of actual diffraction spots obtained through DXT measurement. The right 3D plot of Fig. 2C illustrates angular displacements of the diffraction spots excluding those attributed to physisorption-induced nearly stationary spots and those from frames 0 to 100, as plotted from the left one. Diffraction spots exhibiting minimal mobility due to physisorption are those with average angular speed in the θ or χ directions of less than 0.2 mrad/frame. The exclusion of spots from frames 0 to 100 is justified because immediately after X-ray irradiation, the sample state is often unstable, making it difficult to obtain accurate signals.

Table 1 displays the cumulative diffraction spot numbers for the three variants, obtained by tracking from the measurement data. The analysis utilized diffraction spots obtained by tracking for each variant, excluding spots that remained nearly stationary due to physical adsorption and spots up to the 100th frame after X-ray irradiation. The increasing trend in the number of diffraction spots from omicron, delta,

Table 1
Diffraction spot number of spike variant alpha (B.1.1.7), delta (B.1.617) and omicron (B.1.1.529) with or without ACE2 before filtering or after filtering.

	before filtering	almost stationary	within the initial 100 frames	after filtering
B.1.1.7	1724	727	405	1329
B.1.617	2056	766	453	1596
B.1.1.529	1699	568	261	1434
B.1.1.7 with ACE2	5315	2219	828	2537
B.1.617 with ACE2	7353	2741	1239	3753
B.1.1.529 with ACE2	7695	2811	1234	4092

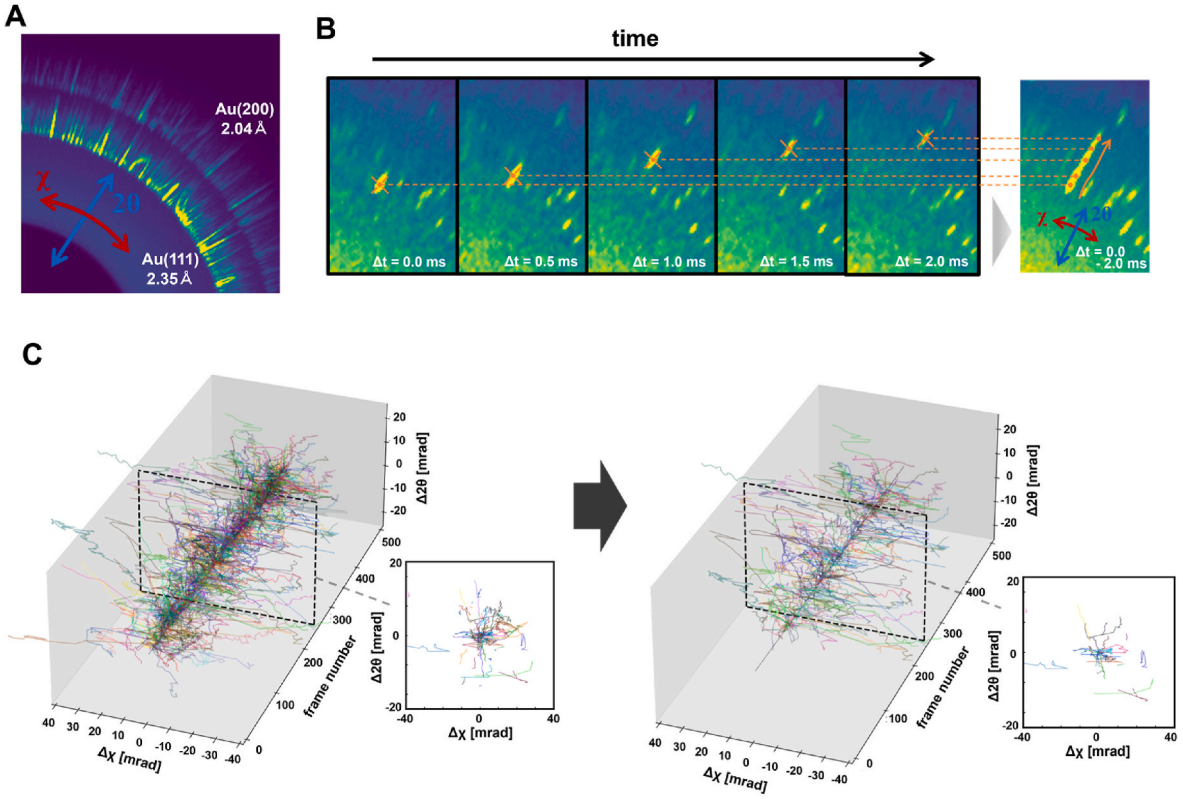

Fig. 2. Tracking of diffraction spots in DXT measurement. **A:** Diffraction image of Au (111) and (200) from gold nanocrystals in DXT measurement. **B:** Tracking displacement of time-varying diffraction spots independently in both tilting (θ) and twisting (χ) directions. **C:** 3D graph plotting the displacement changes of each diffraction spot, with Δχ in the x-direction [mrad], frame number in the y-direction, and Δ2θ in the z-direction [mrad]. (For interpretation of the references to colour in this figure legend, the reader is referred to the Web version of this article.)

to alpha suggests that the binding efficiency between the spike protein and ACE2 is highest for omicron [35]. We calculated the angular displacements for each diffraction spot up to 20 frames and plotted the Mean Square Displacement (MSD) curve for each frame in Fig. 3A. The vertical axis represents the MSD values, and the horizontal axis represents time, ranging from 0 to 2.0 ms (20 frames). In the MSD curves in the θ direction, B.1.617 (blue plots, delta variant) and B.1.1.529 (orange plots, omicron variant) were found to have almost the same mobility. B.1.1.7 (green plot, alpha variant) had slightly lower motion in the θ direction than the others. MSD curves in the χ direction indicates omicron had the most significant rotational motion when compared to the other two variants. Furthermore, when comparing these two mutant strains, the Alpha variant had slightly higher rotational motion than the delta variant. Fig. 3B shows the molecular arrangement of the gold nanocrystals labelled with the SARS-CoV-2 spike trimer at the time when the DXT data in Fig. 3A were collected. The Gold nanocrystals bind to C136 or C488 within the receptor-binding domain (RBD) at the top of the spike protein as shown in Fig. S4. The molecular dynamics in this arrangement indicate the average values of these bindings. It has been reported that C488 plays a crucial role in the cleavage of the spike protein's S1/S2 [36]. Given that the θ and χ directions are components of the polar coordinate representation, it allows for the derivation of a three-dimensional motion summation. In Fig. 3C, the three-dimensional total internal motions of the three variants showed that the omicron variant had the highest motion, followed by the alpha variant, and the delta variant had slightly less motion than the alpha variant. These MSD curves were fitted with the function $r^2(\tau) = D\tau^{\alpha} + b$. $r^2(\tau)$ is MSD [mrad^2], D is the diffusion constant [mrad^2/ms], and τ is the time interval [ms]. The diffusion constant values for alpha, delta, and omicron were 58.5, 61.7, and 71.0 [mrad^2/ms], respectively. Based on these diffusion constant values, the actual travel distances of the three variants were determined based on Fig. S5. The MSD curve is dominated by the

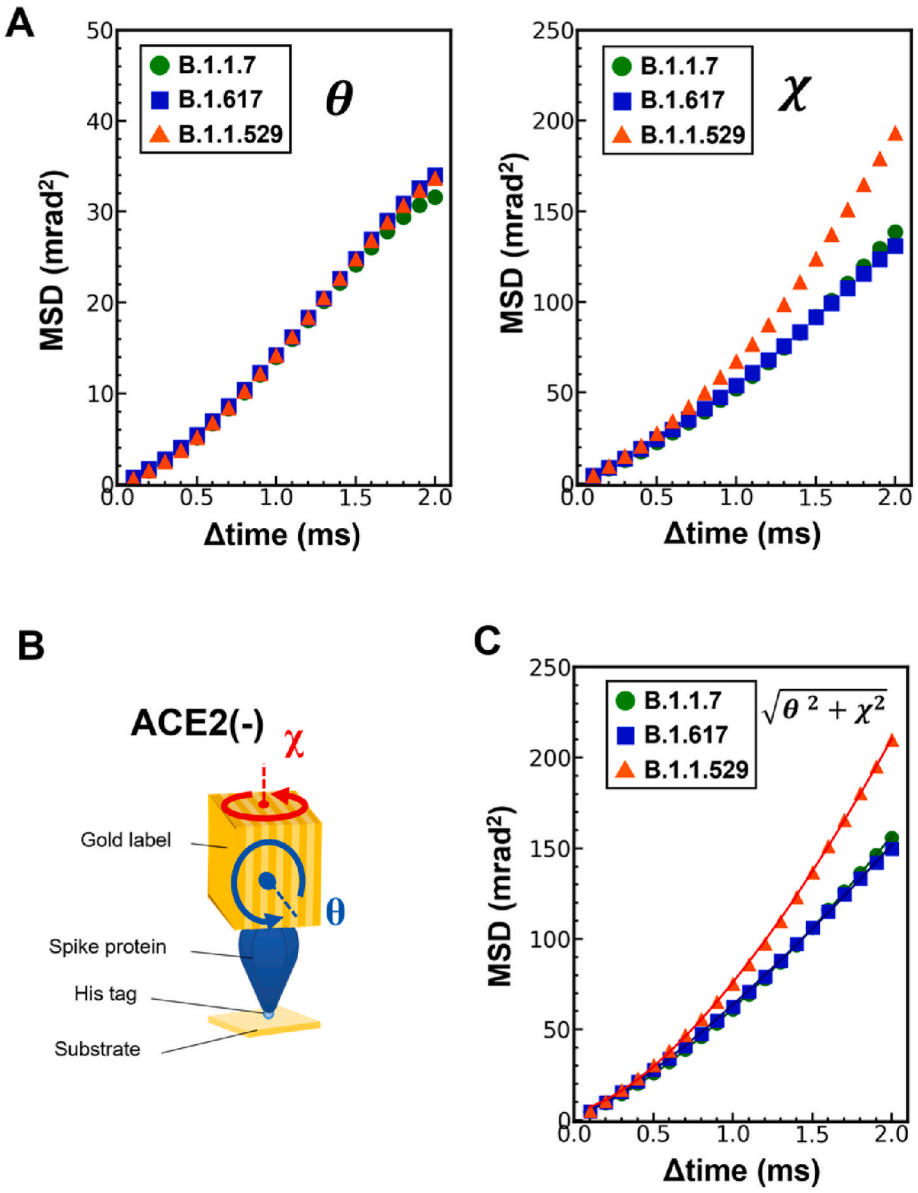

Fig. 3. MSD curves of spike variant alpha (B.1.1.7), delta (B.1.617) and omicron (B.1.1.529) without ACE2. **A:** MSD curves of 3 variants without ACE2 in θ and χ directions, with delay time on the x-axis (20 frames = 2.0 ms) and MSD on the y-axis. **B:** Schematic view of SARS-CoV-2 spike trimer stabilized on a polyimide substrate with a gold nanocrystal. **C:** MSD curves plotting the squared averages in both the θ and χ directions. Fittings was performed on this MSD using the equation $\boldsymbol{r^2(\tau) = D\tau^{\alpha} + b}$. The calculated parameters are presented in Table S1. (For interpretation of the references to colour in this figure legend, the reader is referred to the Web version of this article.)

values in the χ direction. These results suggest that the magnitude of 3-D molecular internal motion can serve as a new factor when discussing the relationship between the magnitude of molecular motion and variants with different infectivity, and the interaction between the virus and the cell.

We show the distribution of angular displacements for the three variants at the 20th frame (Δt = 2.0 ms) in Fig. 3C using boxplots, as shown in Fig. 4A. P-values for each distribution were calculated using the Wilcoxon rank sum test. While no significant difference was observed between alpha and delta, both alpha and omicron, as well as delta and omicron, exhibited statistically significant differences with three asterisks. Fig. 4B presents histograms of the distributions for the three variants, and an overlay of the three histograms is displayed at the bottom. Gaussian curves were used to fit the histogram distributions, and the peak positions were identified individually. Specifically, the distributions of three variants can be fitted with a single Gaussian, indicating the presence of a single mode of motion. These results suggest that the motion of the omicron spike protein is the most pronounced based on the measurements. This outcome implies a potential influence of the binding strength of the omicron spike protein during trimer formation [35,37].

Table 1 shows the cumulative diffraction spot numbers tracked in the spike proteins bound with ACE2, similar to Table 1. Analysis was conducted on diffraction spots, excluding those affected by physical adsorption and the initial 100 frames. As in Fig. 3A, we plotted MSD curves in the θ and χ directions for the system of the spike protein bound to ACE2 in Fig. 5A. In θ direction, The MSD curve for B.1.1.529 is positioned above the other two curves, indicating that B.1.1.529 exhibits the highest mobility. B.1.1.7 and B.1.617 have similar values, suggesting that their motion is comparable. As for the χ direction, the three variants displayed distinct MSD curves. B.1.1.529 had the highest mobility, followed by B.1.617, and then B.1.1.7. The sample arrangement in this measurement was as shown in Fig. 5B, where a trimer of spike proteins immobilized on a substrate with ACE2 was bound with gold nanocrystals. In this arrangement, due to the 100 μs timescale, we measured the molecular dynamics of the interaction between the RBD of the spike protein and ACE2, rather than the overall molecular dynamics of spike protein and ACE2 [38]. We took the square root of the mean square values of the MSD curves in the θ and χ directions in Fig. 5A to calculate the three-dimensional motion (Fig. 5C). This MSD curves show the three-dimensional total internal motions of the three variants with ACE2. The three variants have different motion speed. The largest is omicron, followed by delta, and then alpha. The MSD curve is primarily influenced by values in the χ direction. As in Fig. 3C, these MSD curves were fitted with the function $r^2(\tau) = D\tau^{\alpha} + b$. The diffusion constant values for alpha, delta, and omicron with ACE2 were 57.0, 65.5, and 91.1 [mrad^2/ms], respectively. From the diffusion constant values, the actual travel distances of the three variants were calculated in Table S1.

As in Fig. 5A, we represented the distribution of MSD at the 20th frame (Δt = 2.0 ms) using boxplots (Fig. 6A) and histograms (Fig. 6B) the three variants. For each variant's distribution, a Wilcoxon rank-sum test was performed, and p-values were calculated. Significant differences were observed in all combinations of alpha and delta, delta and omicron, as well as alpha and omicron. This indicates that the three

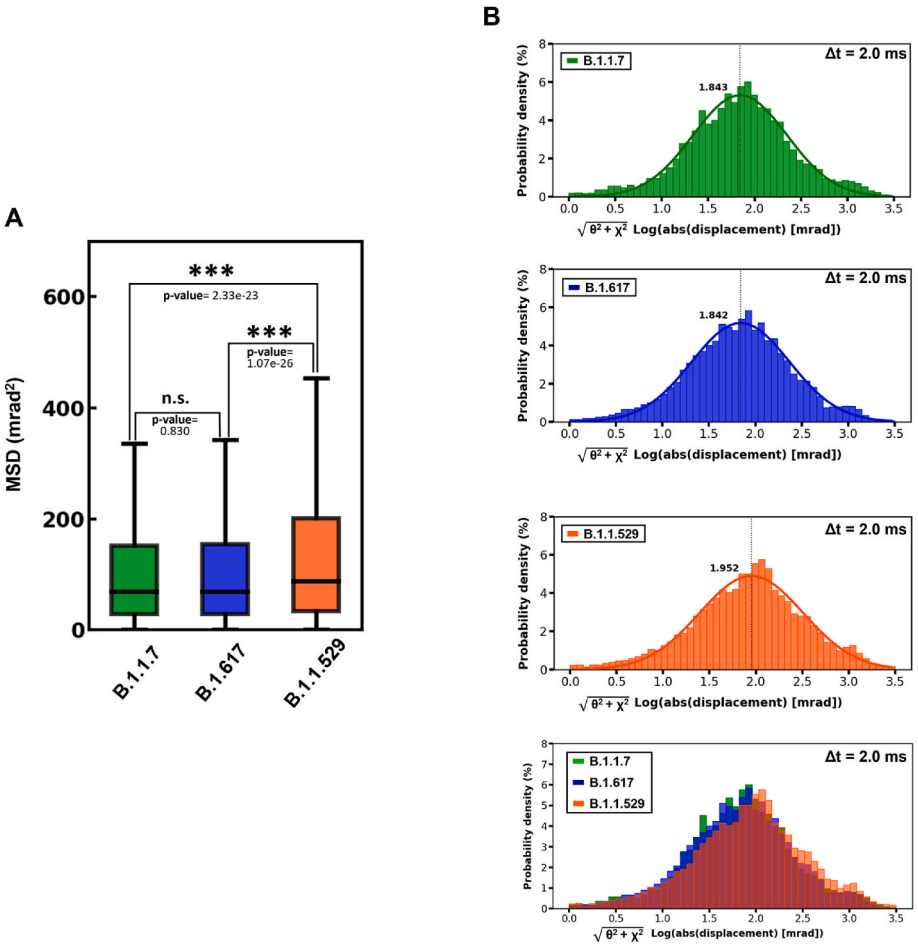

Fig. 4. Boxplot and histograms of alpha (B.1.1.7), delta (B.1.617) and omicron (B.1.1.529) at the 20th frame of the MSD curve in Fig. 3C. **A:** Boxplots for the alpha, delta, and omicron variants without ACE2 were subjected to a Wilcoxon rank sum test (***p-value <0.001, **p-value <0.01, *p-value <0.05). **B:** The histograms of alpha, delta, and omicron with Gaussian fits, and the overlay of the three histograms.

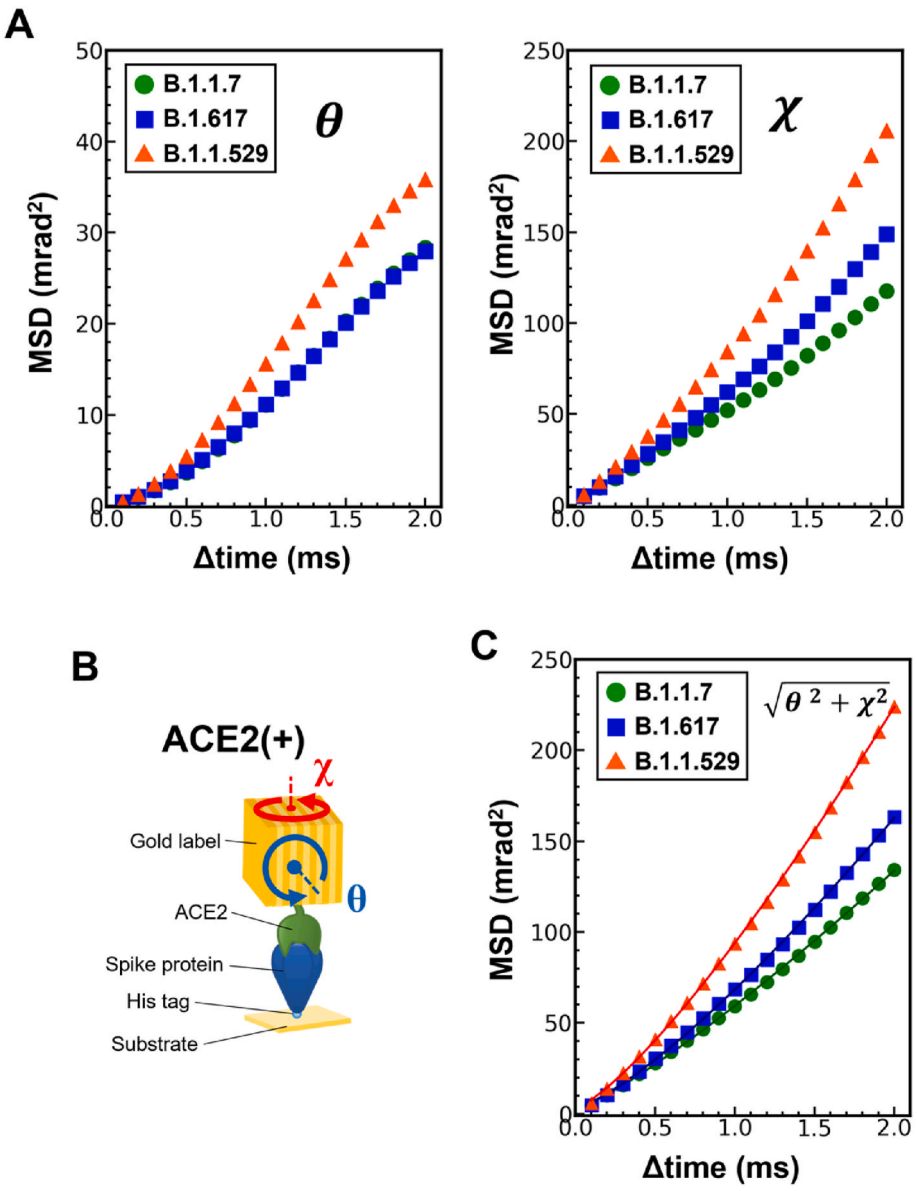

Fig. 5. MSD curves of spike variant alpha (B.1.1.7), delta (B.1.617) and omicron (B.1.1.529) with ACE2. **A:** MSD curves of 3 variants with ACE2 in θ and χ directions, with delay time on the x-axis (20 frames = 2.0 ms) and MSD on the y-axis. **B:** Schematic view of SARS-CoV-2 spike trimer attached to ACE2 with a gold nanocrystal stabilized on a polyimide substrate. **C:** MSD curves plotting the squared averages in both the θ and χ directions. Fittings was performed on this MSD using the equation $r^2(\tau) = D\tau^{\alpha} + b$. The calculated parameters are presented in Table S1. (For interpretation of the references to colour in this figure legend, the reader is referred to the Web version of this article.)

variants exhibit different patterns of dynamics. Fig. 6B represents the distribution of mobility for the three mutant strains in the form of histograms. The histogram distributions were fitted with Gaussian curves, and the peak positions were determined for each. As in Fig. 3B, these distributions of dynamics are also fitted with a single Gaussian. A superimposed representation of the three histograms is provided at the bottom. From these results, it can be inferred that the omicron spike protein, which binds to ACE2, exhibits increased mobility, in agreement with reports of the omicron variant displaying a flexible interaction regime with ACE2, and not contradicting them [39].

3. Summary

Our results suggest Spike protein omicron variants has higher molecular dynamics both on its own and when binding to ACE2 compared to the alpha and delta variants. Furthermore, it also exhibits the characteristic of increased mobility after binding to ACE2. These features suggest that the omicron variant may influence the molecular recognition process following the binding of the spike protein to ACE2.

4. Materials and methods

4.1. Sample preparation

The three variants of SARS-CoV-2 spike protein (B.1.1.7: alpha (#SPN-C52H6, ACRO Biosystems), B.1.617: delta (#SPN-C52Hr, ACRO Biosystems), B.1.1.529: omicron (#SPN-C52 Hz, ACRO Biosystems)) were immobilized via Co^{2+} on polyimide films (thickness: 12 μm) hydrophilized by UV irradiation. Each spike variant was adsorbed by placing 10 μL drops on the substrate at room temperature and incubated for 1 h. In the first experiment, crystalline gold nanocrystals 60–80 nm in diameter were reacted with each adsorbed variant for 30 min under boric acid solution (pH 9.0, 100 mM). The gold nanocrystals can react directly with the cysteine residues of the spike variant. In the next

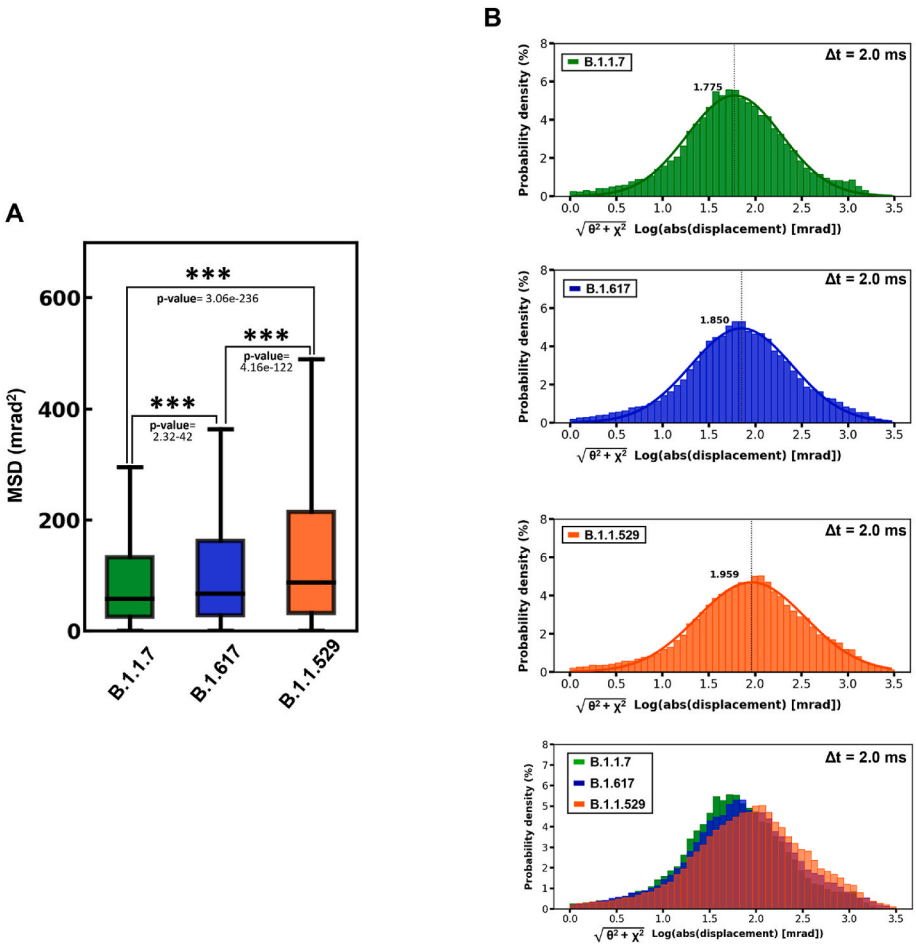

Fig. 6. Boxplot and histogram of spike variant alpha (B.1.1.7), delta (B.1.617) and omicron (B.1.1.529) at the 20th frame of the MSD curve in Fig. 5C. **A:** Boxplots for the alpha, delta, and omicron variants with ACE2 were subjected to a Wilcoxon rank sum test (***p-value <0.001, **p-value <0.01, *p-value <0.05). **B:** The histograms of alpha, delta, and omicron with Gaussian fits, and the overlay of the three histograms.

experiment, spike variants were adsorbed on the substrate as in the previous experiment, ACE2 receptor (#AC2-H5257, ACRO Biosystems, 50 mg/0.1 mL) was reacted with the spike-variant-adsorbed substrate for 1 h, and then gold nanocrystals coated with FC antibody were reacted with the FC-tag in the ACE2 receptor with incubation time for 30 min. Each reaction step was followed by rinsing with buffer solution (PBS, pH 7.5) several times to ensure that unreacted material did not interfere with the single molecule dynamic measurements. DXT measurements were performed by dropping 3 μL of buffer onto the sample substrate and covering it with polyimide films (thickness: 5 μm).

4.2. *Diffracted X-ray Tracking (DXT)*

In this research, DXT was performed in SPring-8 BL40XU using X-rays with energy widths ranging from 14.0 to 16.5 keV and a photon flux of 10^{13} photons/s. The beam size of the incident X-ray was adjusted to 50 μm in diameter by a pinhole slit. The diffraction images by gold nanocrystals were recorded by an X-ray image intensifier (100 mm in diameter, v7339P, Hamamatsu Photonics, Japan) and CMOS camera (Phantom V2511, Vision Research). The distance from the detector to the sample was set to 50 mm. This measurement was performed three times (at 5 × 5 positions per sample), and a total of 75 diffraction data points were obtained for each variant. In DXT analysis of the diffraction spot tracks and trajectories, diffraction spots on the Au (111) surface of gold nanocrystals were tracked by TrackPy (v0.3.2 https://doi.org/10.5281/zenodo.-60550), and custom software written for IGOR Pro (Wavemetrics, Lake Oswego, OR) was used. The analysis was performed by excluding diffraction spots that hardly moved (diffraction spots where the movement distance was 2.0 mrad or less in 20 frames).

Use of experimental human participants

This article does not contain any studies with human participants or human sample performed by any of the authors.

CRediT authorship contribution statement

Daisuke Sasaki: Data curation, Formal analysis, Software, Writing – original draft, Writing – review & editing. **Tatsuya Arai:** Data curation, Software. **Yue Yang:** Formal analysis. **Masahiro Kuramochi:** Software. **Wakako Furuyama:** Conceptualization, Methodology. **Asuka Nanbo:** Conceptualization, Methodology. **Hiroshi Sekiguchi:** Methodology, Software, Data curation. **Nobuhiro Morone:** Conceptualization. **Kazuhiro Mio:** Conceptualization, Data curation, Methodology. **Yuji C. Sasaki:** Conceptualization, Data curation, Funding acquisition, Methodology, Project administration, Supervision, Writing – review & editing.

Declaration of competing interest

The authors declare the following financial interests/personal relationships which may be considered as potential competing interests:

Yuji C. Sasaki reports financial support was provided by Japan Science and Technology Agency. If there are other authors, they declare

that they have no known competing financial interests or personal relationships that could have appeared to influence the work reported in this paper.

Data availability

Data will be made available on request.

Acknowledgements

This work was supported by Ms. R. Kanou, JST CREST (Grant Number: JP18071859, Japan), Japan Agency for Medical Research and Development (AMED) Japan Program for Infectious Diseases Research and Infrastructure (Interdisciplinary Cutting-edge Research, Grant Number: 22wm0325033) and the World-leading Innovative Graduate Study Program in Proactive Environmental Studies (WINGS-PES). Additionally, this work was partly conducted in the cooperative research project program of the National Research Center for the Control and Prevention of Infectious Diseases, Nagasaki University. DXT experiments were performed with the approval of the Japan Synchrotron Radiation Research Institute (Proposal Nos 2018B1435, 2020A2022, 2021B1393 and 2022A1337).

Appendix A. Supplementary data

Supplementary data to this article can be found online at https://doi.org/10.1016/j.bbrep.2024.101712.

References

[1] C. Huang, Y. Wang, X. Li, L. Ren, J. Zhao, Y. Hu, L. Zhang, G. Fan, J. Xu, X. Gu, Z. Cheng, T. Yu, J. Xia, Y. Wei, W. Wu, X. Xie, W. Yin, H. Li, M. Liu, Y. Xiao, H. Gao, L. Guo, J. Xie, G. Wang, R. Jiang, Z. Gao, Q. Jin, J. Wang, B. Cao, Clinical features of patients infected with 2019 novel coronavirus in Wuhan, China, Lancet 395 (2020) 497–506, https://doi.org/10.1016/S0140-6736(20)30183-5.

[2] G. Lippi, C. Mattiuzzi, B.M. Henry, Updated picture of SARS-CoV-2 variants and mutations, Diagnosis 9 (2022) 11–17, https://doi.org/10.1515/dx-2021-0149.

[3] C. Jung, D. Kmiec, L. Koepke, F. Zech, T. Jacob, K.M.J. Sparrer, F. Kirchhoff, Omicron: what makes the latest SARS-CoV-2 variant of concern so concerning?. https://covariants.org/variants/21K.Omicron, 2022.

[4] N. Magazine, T. Zhang, Y. Wu, M.C. McGee, G. Veggiani, W. Huang, Mutations and evolution of the SARS-CoV-2 spike protein, Viruses 14 (2022) 640, https://doi.org/10.3390/v14030640.

[5] D. Wrapp, N. Wang, K.S. Corbett, J.A. Goldsmith, C.-L. Hsieh, O. Abiona, B. S. Graham, J.S. Mclellan, Cryo-EM structure of the 2019-nCoV spike in the prefusion conformation. https://www.science.org, 2019.

[6] A.C. Walls, Y.J. Park, M.A. Tortorici, A. Wall, A.T. McGuire, D. Veesler, Structure, function, and antigenicity of the SARS-CoV-2 spike glycoprotein, Cell. 181 (2020) 281–292.e6, https://doi.org/10.1016/j.cell.2020.02.058.

[7] W. Li, M.J. Moore, N. Vasilieva, J. Sui, S.K. Wong, M.A. Berng, M. Somasundaran, J.L. Sullivan, K. Luzutiaga, T.C. Greenough, H. Choe, M. Farzan, Angiotensin-converting enzyme 2 is a functional receptor for the SARS coronavirus, Nature 426 (2003), https://doi.org/10.1038/nature02145, 450-154.

[8] S.M.C. Gobeil, R. Henderson, V. Stalls, K. Janowska, X. Huang, A. May, M. Speakman, E. Beaudoin, K. Manne, D. Li, R. Parks, M. Barr, M. Deyton, M. Martin, K. Mansouri, R.J. Edwards, A. Eaton, D.C. Montefiori, G.D. Sempowski, K.O. Saunders, K. Wiehe, W. Williams, B. Korber, B.F. Haynes, P. Acharya, Structural diversity of the SARS-CoV-2 Omicron spike, Mol. Cell. 82 (2022) 2050–2068.e6, https://doi.org/10.1016/j.molcel.2022.03.028.

[9] Q. Wang, Y. Zhang, L. Wu, S. Niu, C. Song, Z. Zhang, G. Lu, C. Qiao, Y. Hu, K. Y. Yuen, Q. Wang, H. Zhou, J. Yan, J. Qi, Structural and functional basis of SARS-CoV-2 entry by using human ACE2, Cell 181 (2020) 894–904.e9, https://doi.org/10.1016/j.cell.2020.03.045.

[10] T. Zhou, Y. Tsybovsky, J. Gorman, M. Rapp, G. Cerutti, G.Y. Chuang, P. S. Katsamba, J.M. Sampson, A. Schön, J. Bimela, J.C. Boyington, A. Nazzari, A. S. Olia, W. Shi, M. Sastry, T. Stephens, J. Stuckey, I.T. Teng, P. Wang, S. Wang, B. Zhang, R.A. Friesner, D.D. Ho, J.R. Mascola, L. Shapiro, P.D. Kwong, Cryo-EM structures of SARS-CoV-2 spike without and with ACE2 reveal a pH-dependent switch to mediate endosomal positioning of receptor-binding domains, Cell Host Microbe 28 (2020) 867–879.e5, https://doi.org/10.1016/j.chom.2020.11.004.

[11] Z. Xu, X. Kang, P. Han, P. Du, L. Li, A. Zheng, C. Deng, J. Qi, X. Zhao, Q. Wang, K. Liu, G.F. Gao, Binding and structural basis of equine ACE2 to RBDs from SARS-CoV, SARS-CoV-2 and related coronaviruses, Nat. Commun. 13 (2022) 3547, https://doi.org/10.1038/s41467-022-31276-6.

[12] B. Turoňová, M. Sikora, C. Schürmann, W.J. H Hagen, S. Welsch, F.E. C Blanc, S. von Bülow, M. Gecht, K. Bagola, C. Hörner, G. van Zandbergen, J. Landry, N. Trevisan Doimo de Azevedo, S. Mosalaganti, A. Schwarz, R. Covino, M.D. Mühlebach, G. Hummer, J. Krijnse Locker, M. Beck, In situ structural analysis of SARS-CoV-2 spike reveals flexibility mediated by three hinges, n.d. https://www.science.org.

[13] M.A. Díaz-Salinas, Q. Li, M. Ejemel, L. Yurkovetskiy, J. Luban, K. Shen, Y. Wang, J. B. Munro, Conformational dynamics and allosteric modulation of the SARS-CoV-2 spike, Elife 11 (2022), https://doi.org/10.7554/eLife.75433.

[14] M. Lu, P.D. Uchil, W. Li, D. Zheng, D.S. Terry, J. Gorman, W. Shi, B. Zhang, T. Zhou, S. Ding, R. Gasser, J. Prévost, G. Beaudoin-Bussières, S.P. Anand, A. Laumaea, J.R. Grover, L. Liu, D.D. Ho, J.R. Mascola, A. Finzi, P.D. Kwong, S. C. Blanchard, W. Mothes, Real-time conformational dynamics of SARS-CoV-2 spikes on virus particles, Cell Host Microbe 28 (2020) 880–891.e8, https://doi.org/10.1016/j.chom.2020.11.001.

[15] K. Lim, G. Nishide, T. Yoshida, T. Watanabe-Nakayama, A. Kobayashi, M. Hazawa, R. Hanayama, T. Ando, R.W. Wong, Millisecond dynamic of SARS-CoV-2 spike and its interaction with ACE2 receptor and small extracellular vesicles, J. Extracell. Vesicles 10 (2021), https://doi.org/10.1002/jev2.12170.

[16] J. Yang, S.J.L. Petitjean, M. Koehler, Q. Zhang, A.C. Dumitru, W. Chen, S. Derclaye, S.P. Vincent, P. Soumillion, D. Alsteens, Molecular interaction and inhibition of SARS-CoV-2 binding to the ACE2 receptor, Nat. Commun. 11 (2020), https://doi.org/10.1038/s41467-020-18319-6.

[17] M. Koehler, A. Ray, R.A. Moreira, B. Juniku, A.B. Poma, D. Alsteens, Molecular insights into receptor binding energetics and neutralization of SARS-CoV-2 variants, Nat. Commun. 12 (2021), https://doi.org/10.1038/s41467-021-27325-1.

[18] A. Ali, R. Vijayan, Dynamics of the ACE2–SARS-CoV-2/SARS-CoV spike protein interface reveal unique mechanisms, Sci. Rep. 10 (2020), https://doi.org/10.1038/s41598-020-71188-3.

[19] K.E. Choi, J.M. Kim, J. Rhee, A.K. Park, E.J. Kim, N.S. Kang, Molecular dynamics studies on the structural characteristics for the stability prediction of sars-cov-2, Int. J. Mol. Sci. 22 (2021), https://doi.org/10.3390/ijms22168714.

[20] N. Sepay, S. Chakrabarti, M. Afzal, A. Alarifib, D. Mal, Identification of 4-acrylamido-N-(pyridazin-3-yl) benzamide as anti-COVID-19 compound: a DFTB, molecular docking, and molecular dynamics study, RSC Adv. 12 (2022) 24178, https://doi.org/10.1039/D2RA04333E.

[21] A. Kumar, P.R. Arantes, A. Saha, G. Palermo, B.M. Wong, GPU-enhanced DFTB metadynamics for efficiently predicting free energies of biochemical systems, Molecules 28 (2023) 1277, https://doi.org/10.3390/molecules28031277.

[22] Y.C. Sasaki, Y. Suzuki, N. Yagi, S. Adachi, M. Ishibashi, H. Suda, K. Toyota, M. Yanagihara, Tracking of Individual Nanocrystals Using Diffracted X Rays, (n.d).

[23] Y.C. Sasaki, Y. Okumura, S. Adachi, H. Suda, Y. Taniguchi, N. Yagi, Picometer-scale dynamical X-ray imaging of single DNA molecules, Phys. Rev. Lett. 87 (2001), https://doi.org/10.1103/PhysRevLett.87.248102, 248102-1-248102–4.

[24] H. Sekiguchi, Y. Suzuki, Y. Nishino, S. Kobayashi, Y. Shimoyama, W. Cai, K. Nagata, M. Okada, K. Ichiyanagi, N. Ohta, N. Yagi, A. Miyazawa, T. Kubo, Y. C. Sasaki, Real time ligand-induced motion mappings of AChBP and nAChR using X-ray single molecule tracking, Sci. Rep. 4 (2014), https://doi.org/10.1038/srep06384.

[25] K. Mio, M. Ishihara, S. Fujimura, D. Sasaki, S. Nozawa, K. Ichiyanagi, R. Fukaya, S. ichi Adachi, M. Kuramochi, H. Sekiguchi, T. Kubo, Y.C. Sasaki, X-ray-based living-cell motion analysis of individual serotonin receptors, Biochem. Biophys. Res. Commun. 529 (2020) 306–313, https://doi.org/10.1016/j.bbrc.2020.05.200.

[26] K. Mio, S. Fujimura, M. Ishihara, M. Kuramochi, H. Sekiguchi, T. Kubo, Y.C. Sasaki, Living-cell diffracted x-ray tracking analysis confirmed internal salt bridge is critical for ligand-induced twisting motion of serotonin receptors, Int. J. Mol. Sci. 22 (2021), https://doi.org/10.3390/ijms22105285.

[27] C.R. Morton, N.J. Rzechorzek, J.D. Maman, M. Kuramochi, H. Sekiguchi, R. Rambo, Y.C. Sasaki, O.R. Davies, L. Pellegrini, Structural basis for the coiled-coil architecture of human CtIP, (n.d.). https://doi.org/10.1101/2021.03.05.434060.

[28] G. Chaga, J. Hopp, P. Nelson, Immobilized metal ion affinity chromatography on Co 2 +-carboxymethylaspartate-agarose Superflow, as demonstrated by one-step purification of lactate dehydrogenase from chicken breast muscle, Biotechnol. Appl. Biochem. 29 (1999) 19–24, https://doi.org/10.1111/j.1470-8744.1999.tb01144.x.

[29] H. Yao, Y. Sun, Y.Q. Deng, N. Wang, Y. Tan, N.N. Zhang, X.F. Li, C. Kong, Y.P. Xu, Q. Chen, T.S. Cao, H. Zhao, X. Yan, L. Cao, Z. Lv, D. Zhu, R. Feng, N. Wu, W. Zhang, Y. Hu, K. Chen, R.R. Zhang, Q. Lv, S. Sun, Y. Zhou, R. Yan, G. Yang, X. Sun, C. Liu, X. Lu, L. Cheng, H. Qiu, X.Y. Huang, T. Weng, D. Shi, W. Jiang, J. Shao, L. Wang, J. Zhang, T. Jiang, G. Lang, C.F. Qin, L. Li, X. Wang, Rational development of a human antibody cocktail that deploys multiple functions to confer Pan-SARS-CoVs protection, Cell Res. 31 (2021) 25–36, https://doi.org/10.1038/s41422-020-00444-y.

[30] A.B. Vogel, I. Kanevsky, Y. Che, K.A. Swanson, A. Muik, M. Vormehr, L.M. Kranz, K.C. Walzer, S. Hein, A. Güler, J. Loschko, M.S. Maddur, A. Ota-Setlik, K. Tompkins, J. Cole, B.G. Lui, T. Ziegenhals, A. Plaschke, D. Eisel, S.C. Dany, S. Fesser, S. Erbar, F. Bates, D. Schneider, B. Jesionek, B. Sänger, A.K. Wallisch, Y. Feuchter, H. Junginger, S.A. Krumm, A.P. Heinen, P. Adams-Quack, J. Schlereth, S. Schille, C. Kröner, R. de la Caridad Güimil Garcia, T. Hiller, L. Fischer, R. S. Sellers, S. Choudhary, O. Gonzalez, F. Vascotto, M.R. Gutman, J.A. Fontenot, S. Hall-Ursone, K. Brasky, M.C. Griffor, S. Han, A.A.H. Su, J.A. Lees, N.L. Nedoma, E.H. Mashalidis, P.v. Sahasrabudhe, C.Y. Tan, D. Pavliakova, G. Singh, C. Fontes-Garfias, M. Pride, I.L. Scully, T. Ciolino, J. Obregon, M. Gazi, R. Carrion, K. J. Alfson, W.v. Kalina, D. Kaushal, P.Y. Shi, T. Klamp, C. Rosenbaum, A.N. Kuhn, Ö. Türeci, P.R. Dormitzer, K.U. Jansen, U. Sahin, BNT162b vaccines protect rhesus macaques from SARS-CoV-2, Nature 592 (2021) 283–289, https://doi.org/10.1038/s41586-021-03275-y.

[31] C. Stutz, S. Blein, A single mutation increases heavy-chain heterodimer assembly of bispecific antibodies by inducing structural disorder in one homodimer species,

J. Biol. Chem. 295 (2020) 9392–9408, https://doi.org/10.1074/jbc.RA119.012335.
[32] H. Grönbeck, A. Curioni, W. Andreoni, Thiols and disulfides on the Au(111) surface: the headgroup-gold interaction, J. Am. Chem. Soc. 122 (2000) 3839–3842, https://doi.org/10.1021/ja993622x.
[33] I. Bahar, T.R. Lezon, A. Bakan, I.H. Shrivastava, Normal mode analysis of biomolecular structures: functional mechanisms of membrane proteins, Chem. Rev. 110 (2010) 1463–1497, https://doi.org/10.1021/cr900095e.
[34] A. Srivastava, T. Nagai, A. Srivastava, O. Miyashita, F. Tama, Role of computational methods in going beyond x-ray crystallography to explore protein structure and dynamics, Int. J. Mol. Sci. 19 (2018), https://doi.org/10.3390/ijms19113401.
[35] J. Zhang, Y. Cai, C.L. Lavine, H. Peng, H. Zhu, K. Anand, P. Tong, A. Gautam, M. L. Mayer, S. Rits-Volloch, S. Wang, P. Sliz, D.R. Wesemann, W. Yang, M.S. Seaman, J. Lu, T. Xiao, B. Chen, Structural and functional impact by SARS-CoV-2 Omicron spike mutations, Cell Rep. 39 (2022), https://doi.org/10.1016/j.celrep.2022.110729.
[36] Y. Yamamoto, T. Inoue, M. Inoue, M. Murae, M. Fukasawa, M.K. Kaneko, Y. Kato, K. Noguchi, SARS-CoV-2 spike protein mutation at cysteine-488 impairs its golgi localization and intracellular S1/S2 processing, Int. J. Mol. Sci. 23 (2022), https://doi.org/10.3390/ijms232415834.
[37] B. Zheng, Y. Xiao, B. Tong, Y. Mao, R. Ge, F. Tian, X. Dong, P. Zheng, S373P mutation stabilizes the receptor-binding domain of the spike protein, in: Omicron and Promotes Binding, JACS Au, 2023, https://doi.org/10.1021/jacsau.3c00142.
[38] J. Juraszek, L. Rutten, S. Blokland, P. Bouchier, R. Voorzaat, T. Ritschel, M.J. G. Bakkers, L.L.R. Renault, J.P.M. Langedijk, Stabilizing the closed SARS-CoV-2 spike trimer, Nat. Commun. 12 (2021), https://doi.org/10.1038/s41467-020-20321-x.
[39] E. Socher, L. Heger, F. Paulsen, F. Zunke, P. Arnold, Molecular dynamics simulations of the delta and omicron SARS-CoV-2 spike – ACE2 complexes reveal distinct changes between both variants, Comput. Struct. Biotechnol. J. 20 (2022) 1168–1176, https://doi.org/10.1016/j.csbj.2022.02.015.